



CHORUS

This is the accepted manuscript made available via CHORUS. The article has been published as:

Suppression of the spectral weight of topological surface states on the nanoscale via local symmetry breaking

Omur E. Dagdeviren, Subhasish Mandal, Ke Zou, Chao Zhou, Georg H. Simon, Frederick J. Walker, Charles H. Ahn, Udo D. Schwarz, Sohrab Ismail-Beigi, and Eric I. Altman

Phys. Rev. Materials **2**, 114205 — Published 20 November 2018

DOI: [10.1103/PhysRevMaterials.2.114205](https://doi.org/10.1103/PhysRevMaterials.2.114205)

Suppression of the Spectral Weight of Topological Surface States on the Nanoscale via Local Symmetry Breaking

Omur E. Dagdeviren,^{1,2,†} Subhasish Mandal,^{1,3,†} Ke Zou,^{1,3,†} Chao Zhou,^{1,2} Georg H. Simon,^{1,2} Frederick J. Walker,^{1,3} Charles H. Ahn,¹⁻⁴ Udo D. Schwarz,^{1,2,5} Sohrab Ismail-Beigi,^{1,4} and Eric I. Altman^{1,5}*

¹Center for Research on Interface Structures and Phenomena (CRISP), Yale University, New Haven, Connecticut 06520, USA

²Department of Mechanical Engineering and Materials Science, Yale University, New Haven, Connecticut 06520, USA

³Department of Applied Physics, Yale University, New Haven, Connecticut 06520, USA

⁴Department of Physics, Yale University, New Haven, Connecticut 06520, USA

⁵Department of Chemical and Environmental Engineering, Yale University, New Haven, Connecticut 06520, USA

[†]These authors contributed equally to this work

Keywords

topological crystalline insulators, tin telluride, local symmetry breaking, topological surface states, scanning probe spectroscopy

Abstract

In topological crystalline insulators the topological conducting surface states are protected by crystal symmetry, in principle making it possible to pattern nanoscale insulating and conductive motifs solely by breaking local symmetries on an otherwise homogenous, single-phase material. We show using scanning tunneling microscopy/spectroscopy that defects that break local mirror symmetry of SnTe suppress electron tunneling over an energy range as large as the bulk band gap, an order of magnitude larger than that produced globally via magnetic fields or uniform structural perturbations. Complementary *ab initio* calculations show how local symmetry breaking obstructs topological surface states as shown by a threefold reduction of the spectral weight of the topological surface states. The finding highlights the potential benefits of manipulating the surface morphology to create devices that take advantage of the unique properties of topological surface states and can operate at practical temperatures.

I. Introduction

Topological insulators (TIs) have gained much attention due to the unusual nature of their electronic surface states (SS), which are protected against standard electronic perturbations largely by time-reversal symmetry [1-4]. Similarly, topological crystalline insulators (TCIs) have SS that are protected by crystal symmetry along particular directions: SS exist in the form of massless Dirac fermions while the bulk is semiconducting [5-8]. Tin telluride, a heavily studied material due to its electrical, optical, and thermal properties, is a TCI up to at least room temperature [8-11] (*see Ref [12] for details*). Gapless SS have been observed on (001) and (111) SnTe facets, which have mirror symmetry [6, 8-10, 13]. Global perturbations of the SnTe structure that maintain the crystal symmetry shift the Dirac point in momentum space but keep the surface gapless, [10, 14] while asymmetrically straining the crystal perturbs the SS and opens a global gap [15-17].

We use scanning tunneling microscopy/spectroscopy (STM/S) and density functional theory (DFT) to investigate how local symmetry breaking can be used to manipulate the spectral weight of the topological states of a TCI. Our experimental results show that symmetry-breaking defects suppress electron tunneling, spatially spanning nanometer length scales and energetically ranging over the width of the bulk bandgap at room temperature with no external fields. Complementary *ab initio* calculations confirm the suppression of the spectral weight of topological states and imply that local symmetry breaking may lead to coexisting massive Dirac fermions together with massless Dirac fermions. Decreasing the densities of states by locally perturbing the surface structure is alluring as it permits the patterning of insulating and

conducting regions in the same material, e.g., via a scanning probe tip or annealing in vacuum,[18] essential to forming devices. Moreover, the restricted scattering and spin-locked nature of the topological SS [9] opens horizons for new types of transistors, quantum-dots, microwave circuits, and spin-orbit based devices [19-21].

II. Methods

A. Experimental

Tin telluride films were grown on SrTiO₃ (001) since prior work showed that growth on SrTiO₃ yielded SnTe surfaces with regular defects that could be exploited to investigate the effect of symmetry breaking defects on the surface states of TCIs [22]. The substrates were undoped, single-crystalline SrTiO₃ (001) samples supplied by CrysTec GmbH, Germany that had been etched at the company with buffered HF solution to yield single-terminated surfaces [22-24]. Once in our laboratory, the SrTiO₃ substrates were annealed in ultra-high vacuum for 30 minutes at 1000 K to remove carbon contamination induced by sample transfer through air [24, 25] while remaining non-conducting for any practical scanning tunneling microscopy experiment [24]. The subsequent SnTe film growth was carried out in background pressures below 1×10^{-9} mbar using a molecular beam epitaxy system detailed elsewhere [22]. Single-crystalline SnTe (99.995%) supplied by Alfa Aesar was used as source material for epitaxial growth and was thermally sublimed for 30 minutes from an effusion cell at 820 K. The growth rate was monitored by a quartz microbalance and was held at 2-unit cells (1.26 nm) per minute. The SrTiO₃ substrate was maintained at 670 K during SnTe deposition. Following growth, the film was capped with 20 nm of amorphous Se to protect the sample during sample transfer through

ambient conditions to the vacuum systems in which the surface analysis was being carried out.

After the sample had been re-introduced into vacuum, the Se-capped SnTe film was annealed at 525 K with a background pressure of $\sim 1 \times 10^{-11}$ mbar for 10 - 30 min to decap the Se layer. The temperature was measured with a thermocouple attached next to the sample holder. Following this process, LEED patterns such as the one in Figure S.I.1 revealed that the film exposed SnTe (001) surfaces while Auger electron spectra (cf. Figure S.I.2 for an example) confirmed that the Se was entirely removed.

With clean samples at hand, STM experiments were carried out in UHV and at room temperature using two distinct systems, details of which have been given elsewhere [26-28]. One system was used to collect wider range images with electrochemically etched W tips at tunneling currents up to 0.5 nA while the other was used for atomic resolution imaging and tunneling spectroscopy with Pt-Ir tips and tunneling currents between 6 - 50 pA. The tunneling spectra were collected by recording current and finding the numerical derivative of tunneling current. The set point prior to all tunneling spectroscopy experiments was 30 pA with a -200 mV bias voltage applied to the sample with respect to the tip (hence, changes in the tunneling set point cannot account for the observed differences in the tunneling spectra). Throughout the paper, we use the convention that negative sample bias voltages reflect electron tunneling from the sample to the tip.

B. Computational

Density functional theory (DFT) calculations for SnTe were performed within the generalized gradient approximation of Perdew-Burke-Ernzerhof for exchange and

correlation [29] using the projected augmented wave (PAW) approach as implemented in the QUANTUM ESPRESSO software [30]. Fully relativistic pseudopotentials were employed for both Sn and Te atoms. The plane wave kinetic energy cutoff was set to 30 Ry with a corresponding charge density cutoff of 300 Ry. The theoretically optimized bulk SnTe lattice constant was 6.375 Å, which matches very well the experimental value of 6.35 Å. The bulk band gap with spin-orbit interactions included was comparable to the literature value of 0.19 eV and the gap was found to change as a function of lattice constant similar to literature [8]. A supercell slab method was applied to calculate the band structures and density of states of the surface states. Atoms in the slabs were fixed to their bulk positions.

For all the slab calculations in this work, a minimum of 25 Å of vacuum was included in the simulation cell along (001) to isolate periodic copies. For the stepped structures, the Brillouin zone was sampled by a uniform $4\times 4\times 2$ mesh for self-consistent calculations and a $10\times 7\times 2$ mesh for computing the density of states (DOS). For defect-free surfaces, $6\times 6\times 1$ and $20\times 20\times 1$ meshes of k points (for a 1×1 surface unit cell) were used for self-consistent and DOS calculations, respectively. The Brillouin zone integration was smoothed via the Gaussian smearing technique with a smearing width of 5 mRy (0.068 eV); the same value was used when computing local or projected densities of states.

III. Results

This work focuses on thick tin telluride films (400 unit-cells or ≈ 253 nm) exposing (001) surfaces; at this thickness, the film surfaces exhibit the same structure as the (001) surface of bulk SnTe with X-ray diffraction showing no evidence of strain [18]. Figure 1

(and Figures S.I. 1 and 4) show STM images of (001) flat terraces as large as 10000 nm^2 separated by half unit-cell high steps and free of defects other than Sn vacancies common on this material that shift the position the position of the Fermi level but do not impact TCI properties [6]. Complementary Auger electron spectroscopy experiments (Ref. [18] and Figure S.I 2), together with our STM images, reveal no evidence of surface contamination. Thus, the experiments focus on the clean (001) surface of bulk SnTe known to exhibit TCI properties [8-10].

Although the wide terraces are atomically flat with large apparently perfect regions, defects are evident over greater length scales: e.g., region I in Figure 1a shows a screw dislocation, and region II threading-type screw dislocations that initiate and terminate on the surface. While screw dislocations in TIs do not disrupt topological SS and can even promote the formation of 1D protected states in the bulk [31], they break the C_4 mirror symmetry required for gapless TCI SS and thus may be expected suppress the topological SS on SnTe. In addition, ultra-high vacuum annealing which induced slow, partial sublimation of the film created periodic arrays of pits nucleated at dislocations introduced by small angle boundaries in the epitaxial films (See S.I for more information about pits) [18]. While defects are usually avoided when studying intrinsic materials properties, here we use the surface defects as a platform to reveal their effect on local topological surface properties.

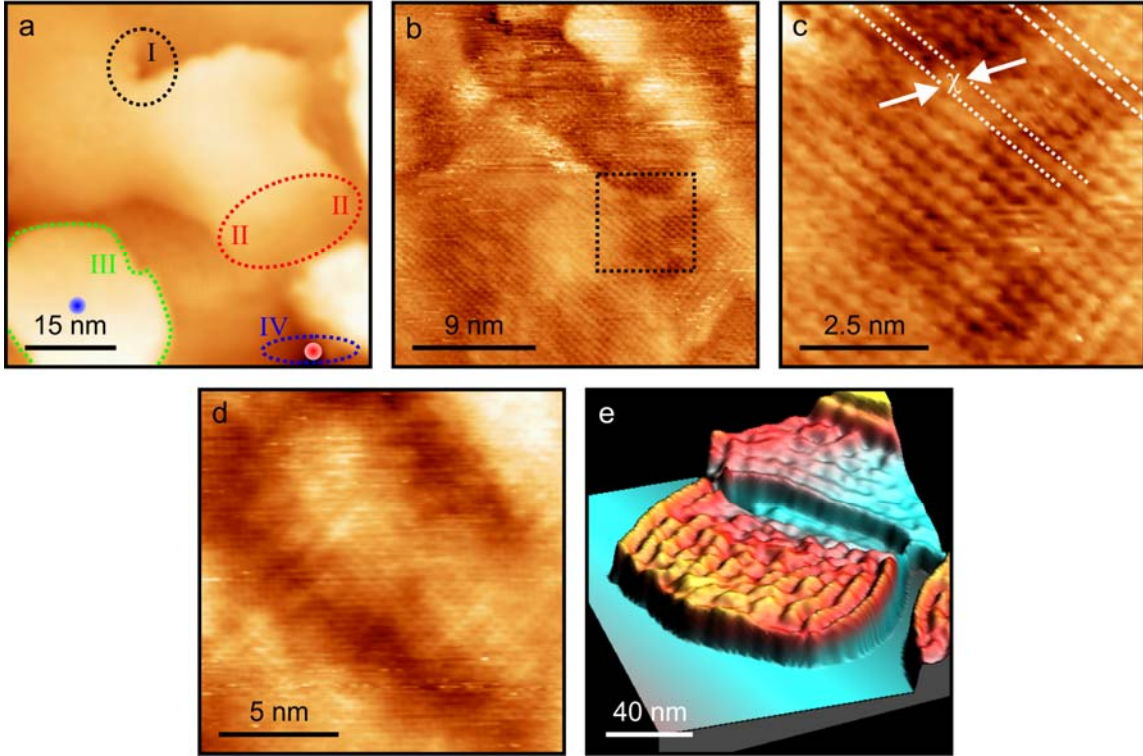


Figure 1: Scanning tunneling microscopy images of a SnTe film grown on SrTiO₃. **(a)** Overview image ($U_{\text{bias}} = 2.2$ V) demonstrates atomically flat terraces with half-unit cell step heights (3.2 Å). The ellipses highlight: (I) a screw dislocation; (II) paired threading screw dislocations; (III) an island; and (IV) a pit. **(b)** A screw dislocation at atomic resolution (200 mV) showing broken mirror symmetry. **(c)** Zoomed in view of the screw dislocation (200 mV) with the dashed lines and chi showing the half unit cell shift of the atomic rows across the dislocation core, while dashed lines at the corner of the image shows unperturbed lines of atoms (see Figure S.I. 6 for further analysis). **(d)** Atomic resolution image (-100 mV) recorded close to a step edge showing superimposed standing waves that have been reported on topological insulator surfaces [32]. **(e)** Three-dimensionally rendered STM topography showing Standing waves induced by step edges (-750 mV). Valley (black)-to-peak (white) corrugations are 14.81 Å (a), 3.67 Å (b), 2.05 Å (c), 4.66 Å (d), and the base to topmost height is 18.54 Å for (e).

The images in Fig. 1b – d show several of the characteristic defects at higher resolution. In particular, screw dislocations were imaged with atomic resolution (Figs. 1b & 1c), which reveals that the broken local symmetry near the dislocation core laterally shifts the atomic rows by half a surface unit cell (arrows and dotted lines in Fig. 1c). In addition, Fig. 1b, c show obvious contrast differences between even nominally identical surface sites. This background contrast can be ascribed to electron scattering and modification of the local density of states (LDOS) by surface imperfections: Figure 1d displays a periodic perturbation of the heights of the atoms while the longer-ranged image in Fig. 1e shows standing wave patterns emanating from step edges and with a 5.5 nm wavelength and a wave vector perpendicular to the step edges (further details on the standing waves can be found in Ref [12]). Quasiparticle scattering of topological SnTe states in this energy range has been previously reported [33].

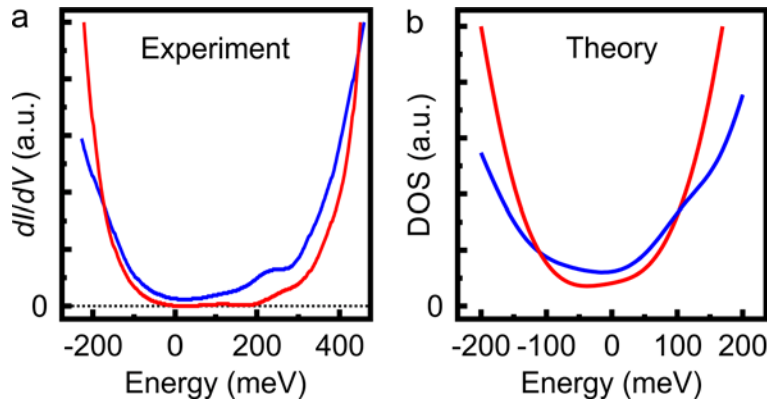


Figure 2: (a) Tunneling spectra recorded in the middle of a terrace (blue curve recorded within the blue circle in region III of Figure 1a) showing densities of states for a defect-free region, and at an area with high curvature (red curve recorded within red circle in region IV of Figure 1a) revealing suppression of densities of states. (b) DFT calculated atom-projected DOS averaged over all surface atoms on the surface layer for infinite terraces (blue) and a stepped vicinal (103)

surface (red) showing suppressed DOS within 50 meV of the Fermi level. These results are for 19-layer thick slabs.

The results in Fig. 1 reveal that defects create electronic contrast in STM images on the 1 – 10 nm length scale. To distinguish the impact of defects on the topological SS, scanning tunneling spectroscopy (STS) experiments were carried out. Conductance (dI/dV) maps recorded as a function of bias voltage at low temperatures are generally used to reveal the local electronic properties [10, 15, 16]. We used a point spectroscopy approach for quantitative analysis of local electronic properties because prior combined STM/NC-AFM measurements on SnTe showed that the tunneling current only becomes measurable when the tip is so close to the surface that the tip–surface interaction is repulsive, resulting in frequent tip changes in the room temperature experiments [18] that impede collecting dI/dV maps. In the middle of a terrace (blue circle in Figure 1a), STS (Figure 2a) indicates no band gap, as expected. Meanwhile, spectra recorded over the steeply sloped area labeled as region IV in Figure 1a (referred to as a “pit” that we typically find surrounds a dislocation created by a small angle boundary as described above [18] and in Ref [12]) reveal a factor of 10 reduction tunneling conductance implying suppression of the density of states from the Fermi level up to 200 meV [8]. The valence band edge is pinned near the Fermi level due to Sn vacancies that *p*-dope the material [6, 34]. The 200 meV span of the effect is much larger than previously reported intensity shifts due to global symmetry breaking via strain [10, 16]. Figure 3 shows the tunneling spectrum recorded around a different pit, which in this case is part of a periodic array (Figure S.I. 4 a-c) [18]. Figure 3 illustrates how the tunneling conductance (proportional to the LDOS at low bias [35]) increases gradually (spectra at II & III) as the

tip moves away from the pit (location I). The small but finite tunneling conductance around the Fermi level can be associated with thermal broadening in the room temperature measurements as well as the radius of curvature of the tip leading to a contribution to the tunneling current from adjacent conductive areas not directly below the tip, particularly when the tip is positioned within a pit [18]. The edges of the pits are comprised of closely spaced atomic steps and inclined facets that form when the steps merge (see Fig. S.I. 1). Conductance maps recorded with the tunneling bias within the gap region (see Fig. S.I. 1g, h) show limited conductance adjacent to an isolated half-unit cell high step, implying that single atomic steps can also impede the topological surface state.

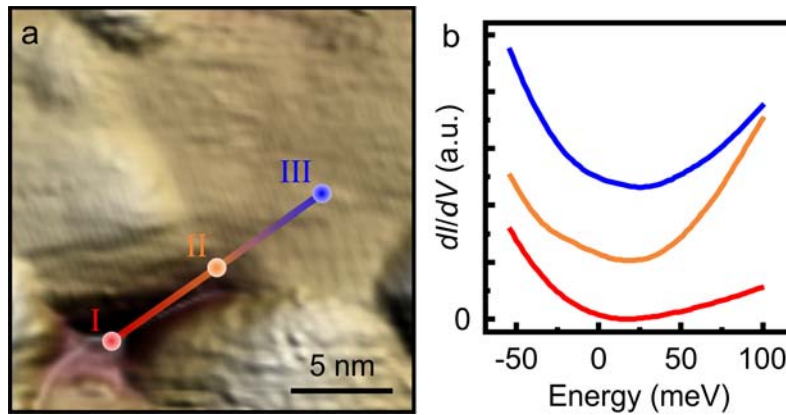


Figure 3: (a) Scanning tunneling microscopy topography image of a pit. (b) Scanning tunneling spectroscopy experiments conducted along a line. Numerical derivative of tunneling spectrum shows that the tunneling conductance is suppressed on top of the pit (I), and gradual increases in dI/dV (II) are observed as the tip moves to smoother regions (III) where mirror symmetry of crystal is protected. Note that the vertical scale of the tunneling spectra is amplified 25 times compared to Fig. 2 (See Fig. S.I. 5 for comparison) to show the variation around the Fermi level more clearly. The valley (black)-to-peak (white) corrugation is 3.41 nm for (a).

We consider and rule out several alternative explanations for the reduced local densities of states. The observed gradual increase in the tunneling conductance around

the Fermi level (up to ≈ 50 meV), which implies an increase in the local density of states with distance from the symmetry breaking zone, could possibly be explained by variations in local chemical composition or undetected tip changes. We did not observe clustering of Sn vacancies on the surface that could create tin telluride phases with a Sn:Te ratio less than one or evidence of impurities in Auger electron spectra [18]. Regarding tip changes, we note that the general features of the spectra are reproducible, i.e. the tip can be moved back and forth between the marked locations multiple times without changes.

The fundamental question we wish to address is if the suppression of the conducting surface states can be attributed to defects disrupting the mirror symmetry: to this end we conducted DFT calculations on model systems. The DFT calculations were done with two prototypical surfaces (detail in SI): one is the ideal flat (001) surface preserving mirror symmetry and the other is the stepped (103) surface, which has periodic surface steps along [100] that break the mirror symmetry between the [100] and [001] directions. The vicinal surface used in the computation contains step edges to replicate the experimental situation, and at the same time its periodic nature makes DFT calculations tractable. Figure 2b highlights a qualitative analysis based on the atomic-orbital projected density of states (PDOS) on the surface atoms: the stepped surface has a noticeably reduced density of states near the Fermi level. Other qualitative spectral features reproduced by theory include a hump near 100 meV for the defect-free surface, which corresponds to Sn p dominated states, seen at 200 meV in the experimental spectrum of Figure 2a (the difference in energy is due to DFT underestimating band gaps and the p -doping of the experimental sample) [36].

The agreement between DFT and experiment in Figure 2 is qualitative with a weaker reduction in the PDOS due to symmetry breaking defects; we discuss three reasons for this discrepancy. First, computing the PDOS requires broadening (smearing) of the discrete set of computed energy levels from the finite simulation size, and our results are based on a Gaussian broadening of 70 meV. Second, a PDOS should not be compared directly and quantitatively to the experimental dI/dV : since tunneling happens in real-space, the real-space local density of states (LDOS) is a better quantitative surrogate for dI/dV and shows a much larger reduction near the Fermi level as illustrated in Figure 4. Third, our simulation cells are too small to distinguish differences of electronic structure between step edges and flat terraces in the same calculation: we have simulated 3-, 5-, and 7-atom wide terraces ($\sim 1-2$ nm wide) and all show reduced surface DOS near the Fermi level (see SI). Given the experimental observation that one must move $\sim 10-15$ nm away from a step edge to recover the clean surface DOS (Figure 3 and SI), the required simulation cells to directly reproduce this effect and isolate the effect of a single step edge are too large for present day DFT calculations.

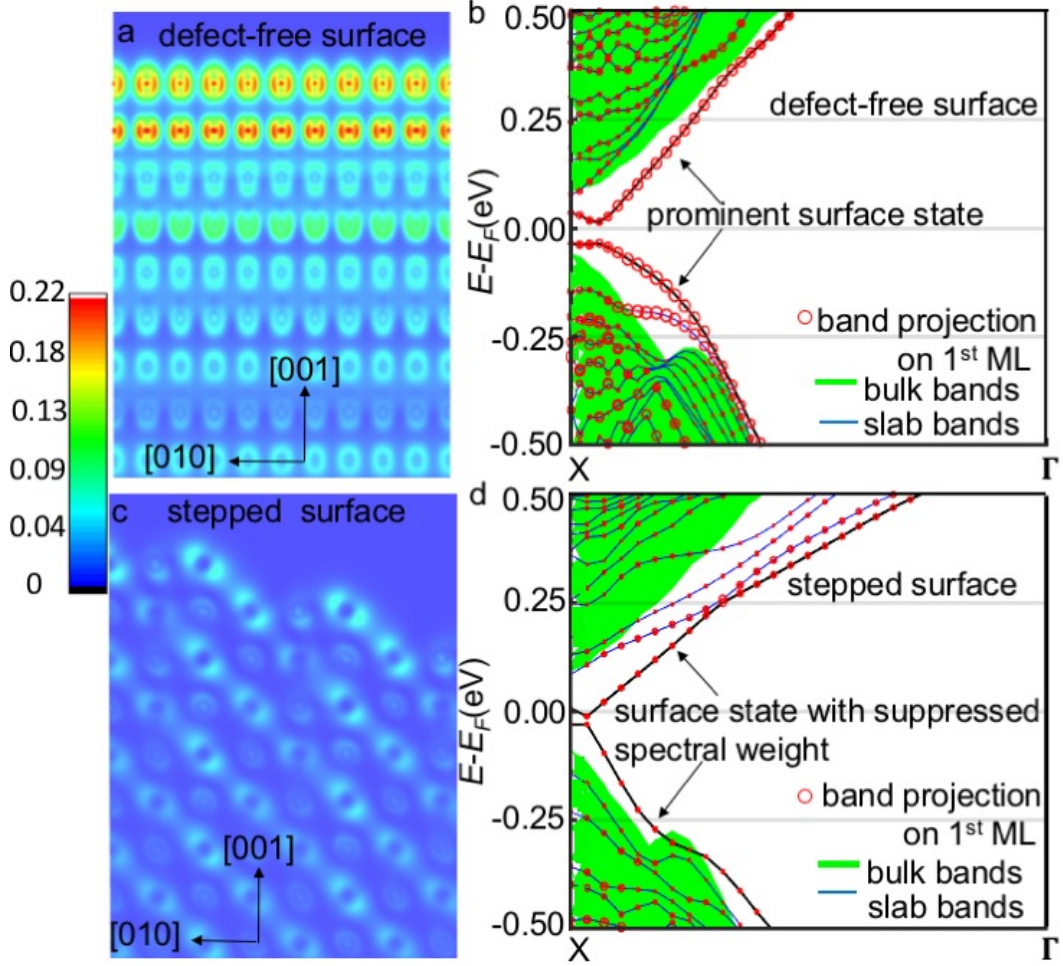


Figure 4: DFT calculations for 19 atomic layers thick (001) SnTe slabs. (a) & (c) Integrated from $E_F - 0.1$ eV to $E_F + 0.1$ eV, capturing predominantly the surface states, and averaged (along [100]) LDOS in real-space for the (a) defect-free and (c) the stepped (001) SnTe surfaces. Higher (lower) LDOS is shown by red (blue) colors on a same color scale plot. (b) & (d) Theoretical band structure for defect-free (c) and stepped surfaces (d); the green-shaded area refers to the bulk bands while blue lines are computed for finite slabs. The SS forming the Dirac point are shown in thick black color with their weight indicated by the size of the red circles (band projection). The SS exists in both cases but the spectral weight of the topological surface states is greatly reduced for the stepped surface. The small gap for the SS in (b) is due to the finite slab thickness [37].

For a better comparison with STM data, Figure 4 shows a comparison of the real-space LDOS for the two model systems on the same scale. The contrast between defect-free and defective surfaces is striking: the LDOS reduction is quite dramatic and is numerically a factor of ~ 3 , which means that the spectral weight of metallic SS have been nearly eliminated by the symmetry-breaking defect. We also note that the atoms protruding at the edges have a much higher LDOS than those in the flat terrace regions of the surface; this chemical effect, due to dangling bonds, is in agreement with how atoms near vacancies appear brighter in the STM images (Fig. S.I.3). This level of detailed agreement gives further confidence regarding the relevance of the modeling.

The DFT band structure of the thick defect-free surface shows the expected Dirac-point near the X-point (Figure 4b and Figure S.I. 7). A very small hybridization gap (< 0.04 eV) appears due to the slab's finite thickness: when the slab thickness is increased from 4 ML to 19 ML, this artificial gap decreases [37] (see Figure S.I.9). The projection of each band on the surface atomic orbitals shows that, as expected, the states near the Dirac point have strong projections on the surface atoms (Figure 4b and Figure S.I. 8). The band structure plot for the symmetry broken stepped surface is provided in Figure 4d. A Dirac point is observable near the Fermi energy, which is due to the existence of flat regions in the simulation, but the surface projections are reduced significantly, indicating the suppression of spectral weight of the topological surface states. These results provide a physical picture of what the band structure of a defective surface with larger flat terraces should look like: the flat regions would support massless Dirac fermions while simultaneously regions near the defects would have greatly suppressed weights for the Dirac bands; if the defective region is wide enough, a gapped spectrum

with massive fermions would be observed inside it. Dirac mass generation by opening up a gap due to *globally* breaking mirror symmetry over an entire crystal was recently demonstrated for $\text{Pb}_{1-x}\text{Sn}_x\text{Te}$ [15]. Here, we argue that Dirac mass generation can potentially be achieved by locally breaking the mirror symmetry on the surface by creating extended defective regions. Hence, the global band structure or the global Dirac points, e.g., as measured by angular-resolved photoemission spectroscopy (ARPES), can remain gapless even though locally gaps can form. From the ARPES viewpoint, the effect of local gap formation is subtle as it simply reduces the spectral weight near the Fermi level compared to the clean surface (see Figure 4). However, local probes can uncover the change of spectral weight directly and dramatically, as described above.

IV. Summary

Experiments and *ab initio* calculations revealed that topological SS in TCIs can be inhibited by local symmetry breaking. The impact of such defects has been exposed experimentally via the observation of suppressed conductance in tunneling spectra recorded within defective regions. Our experimental findings are supported and explained by DFT calculations on a prototypical surface that breaks local mirror symmetry in SnTe and shows spectral weight suppression near the Dirac point. Our results demonstrate that topological SS may be tailored within regions confined to a few nanometers. Such local modification of topological states can be manipulated by *in-situ* heat treatment of epitaxial films [18]. The collapse of gapless SS to a bulk state may enable the fabrication of novel electronic devices operating near room temperature on a single material simply by patterning islands or pits, thereby bypassing complex issues regarding the interactions and compatibilities of different materials across interfaces.

Corresponding Author

*Corresponding author: eric.altman@yale.edu

Acknowledgments

We thank Profs. Leonid Glazman and Judy Cha for fruitful discussions. The research was funded by the Focus Center on Function Accelerated nanoMaterial Engineering (FAME) and the NSF (Grant No. MRSEC DMR-1119826) through the Yale Materials Research Science and Engineering Center. S.M. was supported by the NSF SI2-SSI program (Grant No. ACI-1339804). Computational facilities are supported by NSF XSEDE resources through Grant No. TG-MCA08X007 and by the facilities and staff of the Yale University Faculty of Arts and Sciences High Performance Computing Center.

References

1. M.Z. Hasan and C.L. Kane, Topological insulators. *Reviews of Modern Physics* **82**, 3045-3067 (2010).
2. J.E. Moore, The birth of topological insulators. *Nature* **464**, 194-198 (2010).
3. R.-J. Slager, A. Mesaros, V. Juričić, and J. Zaanen, The space group classification of topological band-insulators. *Nature Physics* **9**, 98 (2012).
4. R.-J. Slager, The translational side of topological band insulators. arXiv:1708.08886 (2017).
5. L. Fu, Topological Crystalline Insulators. *Physical Review Letters* **106**, 106802 (2011).
6. Y. Tanaka, Z. Ren, T. Sato, K. Nakayama, S. Souma, T. Takahashi, K. Segawa, and Y. Ando, Experimental realization of a topological crystalline insulator in SnTe. *Nat Phys* **8**, 800-803 (2012).
7. S.-Y. Xu, C. Liu, N. Alidoust, M. Neupane, D. Qian, I. Belopolski, J.D. Denlinger, Y.J. Wang, H. Lin, L.A. Wray, G. Landolt, B. Slomski, J.H. Dil, A. Marcinkova, E. Morosan, Q. Gibson, R. Sankar, F.C. Chou, R.J. Cava, A. Bansil, and M.Z. Hasan, Observation of a topological crystalline insulator phase and topological phase transition in $\text{Pb}_{1-x}\text{Sn}_x\text{Te}$. *Nat Commun* **3**, 1192 (2012).
8. T.H. Hsieh, H. Lin, J. Liu, W. Duan, A. Bansil, and L. Fu, Topological crystalline insulators in the SnTe material class. *Nat Commun* **3**, 982 (2012).
9. M. Safdar, Q. Wang, M. Mirza, Z. Wang, K. Xu, and J. He, Topological Surface Transport Properties of Single-Crystalline SnTe Nanowire. *Nano Letters* **13**, 5344-5349 (2013).
10. I. Zeljkovic, D. Walkup, B.A. Assaf, K.L. Scipioni, SankarR, F. Chou, and V. Madhavan, Strain engineering Dirac surface states in heteroepitaxial topological crystalline insulator thin films. *Nat Nano* **10**, 849-853 (2015).
11. C.M. Polley, V. Jovic, T.Y. Su, M. Saghir, D. Newby, B.J. Kowalski, R. Jakiela, A. Barcz, M. Guzewicz, T. Balasubramanian, G. Balakrishnan, J. Laverock, and K.E. Smith, Observation of surface states on heavily indium-doped SnTe(111), a superconducting topological crystalline insulator. *Physical Review B* **93**, 075132 (2016).

12. See Supplemental Material at < [web link here](#) > for details concerning SnTe topological properties at room temperature, experimental and computational methods which contain the following references [6, 8, 11, 18, 33, 37-43].
13. J. Shen, Y. Jung, A.S. Disa, F.J. Walker, C.H. Ahn, and J.J. Cha, Synthesis of SnTe Nanoplates with {100} and {111} Surfaces. *Nano Letters* **14**, 4183-4188 (2014).
14. M. Serbyn and L. Fu, Symmetry breaking and Landau quantization in topological crystalline insulators. *Physical Review B* **90**, 035402 (2014).
15. Y. Okada, M. Serbyn, H. Lin, D. Walkup, W. Zhou, C. Dhital, M. Neupane, S. Xu, Y.J. Wang, R. Sankar, F. Chou, A. Bansil, M.Z. Hasan, S.D. Wilson, L. Fu, and V. Madhavan, Observation of Dirac Node Formation and Mass Acquisition in a Topological Crystalline Insulator. *Science* **341**, 1496-1499 (2013).
16. I. Zeljkovic, Y. Okada, M. Serbyn, R. Sankar, D. Walkup, W. Zhou, J. Liu, G. Chang, Y.J. Wang, M.Z. Hasan, F. Chou, H. Lin, A. Bansil, L. Fu, and V. Madhavan, Dirac mass generation from crystal symmetry breaking on the surfaces of topological crystalline insulators. *Nat Mater* **14**, 318-324 (2015).
17. M. Drüppel, P. Krüger, and M. Rohlfing, Strain tuning of Dirac states at the SnTe (001) surface. *Physical Review B* **90**, 155312 (2014).
18. O.E. Dagdeviren, C. Zhou, K. Zou, G.H. Simon, S.D. Albright, S. Mandal, M.D. Morales-Acosta, X. Zhu, S. Ismail-Beigi, F.J. Walker, C.H. Ahn, U.D. Schwarz, and E.I. Altman, Length Scale and Dimensionality of Defects in Epitaxial SnTe Topological Crystalline Insulator Films. *Advanced Materials Interfaces* **4**, 1601011-10 (2017).
19. J.R. Bindel, M. Pezzotta, J. Ulrich, M. Liebmann, E.Y. Sherman, and M. Morgenstern, Probing variations of the Rashba spin-orbit coupling at the nanometre scale. *Nat Phys* **12**, 920-925 (2016).
20. J. Nitta, Spin-orbit coupling: Ready for a close-up. *Nat Phys* **12**, 898-899 (2016).
21. J. Liu, T.H. Hsieh, P. Wei, W. Duan, J. Moodera, and L. Fu, Spin-filtered edge states with an electrically tunable gap in a two-dimensional topological crystalline insulator. *Nat Mater* **13**, 178-183 (2014).
22. K. Zou, S. Mandal, S.D. Albright, R. Peng, Y. Pu, D. Kumah, C. Lau, G.H. Simon, O.E. Dagdeviren, X. He, I. Božović, U.D. Schwarz, E.I. Altman, D. Feng, F.J. Walker, S. Ismail-Beigi, and C.H. Ahn, Role of double TiO₂ layers at the interface of FeSe/SrTiO₃ superconductors. *Physical Review B* **93**, 180506 (2016).
23. M. Kawasaki, K. Takahashi, T. Maeda, R. Tsuchiya, M. Shinohara, O. Ishiyama, T. Yonezawa, M. Yoshimoto, and H. Koinuma, Atomic Control of the SrTiO₃ Crystal Surface. *Science* **266**, 1540-1542 (1994).
24. O.E. Dagdeviren, G.H. Simon, K. Zou, F.J. Walker, C. Ahn, E.I. Altman, and U.D. Schwarz, Surface phase, morphology, and charge distribution transitions on vacuum and ambient annealed SrTiO₃ (100). *Physical Review B* **93**, 195303 (2016).
25. T. Kubo and H. Nozoye, Surface structure of SrTiO₃. *Surface Science* **542**, 177-191 (2003).
26. M. Li and E.I. Altman, Formation and interaction of epitaxial Ge structures on Ge(001). *Physical Review B* **66**, 115313 (2002).
27. B.J. Albers, M. Liebmann, T.C. Schwendemann, M.Z. Baykara, M. Heyde, M. Salmeron, E.I. Altman, and U.D. Schwarz, Combined low-temperature scanning tunneling/atomic force microscope for atomic resolution imaging and site-specific force spectroscopy. *Review of Scientific Instruments* **79**, 033704 (2008).

28. O.E. Dagdeviren, J. Götzen, H. Hölscher, E.I. Altman, and U.D. Schwarz, Robust high-resolution imaging and quantitative force measurement with tuned-oscillator atomic force microscopy. *Nanotechnology* **27**, 065703 (2016).
29. J.P. Perdew, K. Burke, and M. Ernzerhof, Generalized Gradient Approximation Made Simple. *Physical Review Letters* **77**, 3865-3868 (1996).
30. G. Paolo, B. Stefano, B. Nicola, C. Matteo, C. Roberto, C. Carlo, C. Davide, L.C. Guido, C. Matteo, D. Ismaila, C. Andrea Dal, G. Stefano de, F. Stefano, F. Guido, G. Ralph, G. Uwe, G. Christos, K. Anton, L. Michele, M.-S. Layla, M. Nicola, M. Francesco, M. Riccardo, P. Stefano, P. Alfredo, P. Lorenzo, S. Carlo, S. Sandro, S. Gabriele, P.S. Ari, S. Alexander, U. Paolo, and M.W. Renata, QUANTUM ESPRESSO: a modular and open-source software project for quantum simulations of materials. *Journal of Physics: Condensed Matter* **21**, 395502 (2009).
31. Y. Ran, Y. Zhang, and A. Vishwanath, One-dimensional topologically protected modes in topological insulators with lattice dislocations. *Nat Phys* **5**, 298-303 (2009).
32. Z. Alpichshev, J.G. Analytis, J.H. Chu, I.R. Fisher, Y.L. Chen, Z.X. Shen, A. Fang, and A. Kapitulnik, STM Imaging of Electronic Waves on the Surface of Bi_2Te_3 : Topologically Protected Surface States and Hexagonal Warping Effects. *Physical Review Letters* **104**, 016401 (2010).
33. D. Zhang, H. Baek, J. Ha, T. Zhang, J. Wyrick, A.V. Davydov, Y. Kuk, and J.A. Stroscio, Quasiparticle scattering from topological crystalline insulator SnTe (001) surface states. *Physical Review B* **89**, 245445 (2014).
34. P.B. Littlewood, B. Mihaila, R.K. Schulze, D.J. Sarik, J.E. Gubernatis, A. Bostwick, E. Rotenberg, C.P. Opeil, T. Durakiewicz, J.L. Smith, and J.C. Lashley, Band Structure of SnTe Studied by Photoemission Spectroscopy. *Physical Review Letters* **105**, 086404 (2010).
35. J. Tersoff and D.R. Hamann, Theory and Application for the Scanning Tunneling Microscope. *Physical Review Letters* **50**, 1998-2001 (1983).
36. M.S. Hybertsen and S.G. Louie, Electron correlation in semiconductors and insulators: Band gaps and quasiparticle energies. *Physical Review B* **34**, 5390-5413 (1986).
37. S. Liu, Y. Kim, L.Z. Tan, and A.M. Rappe, Strain-Induced Ferroelectric Topological Insulator. *Nano Letters* **16**, 1663-1668 (2016).
38. G. Balakrishnan, L. Bawden, S. Cavendish, and M.R. Lees, Superconducting properties of the In-substituted topological crystalline insulator SnTe . *Physical Review B* **87**, 140507 (2013).
39. H. Preier, Recent advances in lead-chalcogenide diode lasers. *Applied physics* **20**, 189-206 (1979).
40. C.R. Hewes, M.S. Adler, and S.D. Senturia, Nuclear-Magnetic-Resonance Studies in PbTe and SnTe : An Experimental Determination of $\mathbf{k} \cdot \mathbf{p}$ Band Parameters and Magnetic Hyperfine Constants. *Physical Review B* **7**, 5195-5212 (1973).
41. N.W.a.M. Ashcroft, N.D., *Solid State Physics*. 1981, Philadelphia: Saunders College.
42. L.E. Davis, N.C. MacDonald, P.W. Palmberg, G.E. Riach, and R.E. Weber, *A Reference Book of Standard Data for Identification and Interpretation of Auger Electron Spectroscopy Data*. 2nd ed. 1976, Minnesota, USA: Physics Electronics Industries Inc.
43. X. Qian, L. Fu, and J. Li, Topological crystalline insulator nanomembrane with strain-tunable band gap. *Nano Research* **8**, 967-979 (2014).

[6, 8, 11, 18, 33, 37-43]